Direct observation of an extended X-ray jet at *z* = 6.1

L. Ighina[1,2], A. Moretti[1], F. Tavecchio[3], A. Caccianiga[1], S. Belladitta[1,2], D. Dallacasa[4,5], R. Della Ceca[1], T. Sbarrato[3], and C. Spingola[5]

[1] INAF – Osservatorio Astronomico di Brera, via Brera 28, 20121 Milano, Italy
[2] DiSAT – Università degli Studi dell'Insubria, via Valleggio 11, 22100 Como, Italy
   e-mail: lighina@uninsubria.it
[3] INAF – Osservatorio Astronomico di Brera, via E. Bianchi 46, 23807 Merate, Italy
[4] Department of Physics and Astronomy, Università degli Studi di Bologna, Via Gobetti 93/2, 40129 Bologna, Italy
[5] INAF – Institute for Radioastronomy, via Gobetti 101, 40129 Bologna, Italy

Received 16 November 2021 / Accepted 12 January 2022

ABSTRACT

We report on the direct observation of an extended X-ray jet in the $z = 6.1$ radio-loud active galactic nucleus PSO J030 947.49+271757.31 from a deep *Chandra* X-ray observation (128 ksec). This detection represents the most distant kiloparsec-scale off-nuclear emission resolved in X-rays to date. The angular distance of the emission is ~4″ (corresponding to ~20 kpc at $z = 6.1$), along the same direction of the jet observed at parsec scales in previous VLBA high-resolution radio observations. Moreover, the 0.5–7.0 keV isophotes coincide with the extended radio emission as imaged by the VLA Sky Survey at 3 GHz. The rest-frame 2–10 keV luminosity of the extended component is L_{2-10} keV $= 5.9 \times 10^{44}$ erg s^{-1}, about 8% of the core: this makes it one of the most luminous jets resolved in X-rays so far. Through spectral energy distribution modelling we find that this emission can be explained by the inverse Compton interaction with the photons of the cosmic microwave background, assuming that the jet's physical parameters are similar to those in the local Universe. At the same time, we find that the radiation produced by a putative population of high-energy electrons through the synchrotron process observed at low redshift is quenched at high redshift, hence becoming negligible.

Key words. galaxies: active – galaxies: high-redshift – galaxies: jets – quasars: individual: PSO J047.4478+27.2992 – X-rays: general

1. Introduction

Active galactic nuclei (AGNs) are the brightest permanent astronomical objects and one of the most valuable sources of information from the early Universe. A fraction of them (~10–15%; e.g., Liu et al. 2021; Diana et al. 2021) are able to expel part of the accreting matter in the form of two collimated relativistic jets originating very close to the supermassive black hole (SMBH) and extending even up to a few megaparsecs (e.g., Blandford et al. 2019).

Understanding the mechanisms responsible for the launch and emission of these jets is of crucial importance for constraining the kinetic power they carry and therefore their feedback on the intergalactic medium as a function of redshift (e.g., Nesvadba et al. 2007; Fabian 2012). It is also crucial for constraining the cosmological evolution of the SMBHs hosted in jetted AGNs (e.g., Fabian et al. 2014) and the relative contribution of jets to the re-ionisation of the Universe at $z > 6$ (e.g., Torres-Albà et al. 2020).

Even though we are able to resolve the emission and the structure of relativistic jets up to milliarcsecond scales with radio observations (e.g., Boccardi et al. 2017), in X-rays we usually observe only the unresolved emission produced in the innermost compact region of the jet, in particular when it is closely aligned to our line of sight (i.e. blazars; e.g., Bhatta et al. 2018). However, there are a few exceptions where, thanks to the angular resolution of the *Chandra* X-ray telescope (~0.5″; Weisskopf et al. 2000), we are able to resolve the most extended regions of relativistic jets in the X-ray band and therefore study their properties even at high energies.

Nevertheless, more than 20 years after the direct detection and study of the first extended jet observed with the *Chandra* telescope in X-rays (Schwartz et al. 2000), there is no homogeneous consensus on the mechanism responsible for the radiation observed several kiloparsecs away from the SMBH. One of the first and most popular interpretations proposed for the extended high-energy emission is the interaction of electrons with the photons of the cosmic microwave background (CMB) through the inverse Compton (IC) process (IC/CMB; e.g., Tavecchio et al. 2000; Celotti et al. 2001). Despite this model's initial success, the non-detections of a strong and permanent γ-ray emission from sources in the local Universe ($z < 1$) ruled out the possibility that this process is the main contributor to the observed X-ray emission in most objects (e.g., Meyer et al. 2015; Breiding et al. 2017). At the same time, synchrotron emission from a second highly energetic population of electrons, different from the one responsible for the radio emission, seems to be favoured (Harris & Krawczynski 2002; Jester et al. 2002; Georganopoulos et al. 2006). In any case, we still expect the IC/CMB interaction to take place to a certain degree, especially at high redshift, thanks to the strong evolution of the CMB energy density, $\propto (1 + z)^4$ (e.g., Ighina et al. 2021). For this reason, the best way to characterise this interaction and its contribution to the overall X-ray emission is to focus on the high-z jetted AGN population and then extrapolate the expected amount to lower redshifts (Worrall et al. 2020), where many extended jets have already been analysed (e.g., Harris & Krawczynski 2006; Marshall et al. 2011). At the same time, the IC/CMB radiation is also strongly dependent on the viewing angle (more so than the synchrotron radiation; e.g., Worrall 2009) and can therefore

be more easily observed in blazars, where the relativistic jet is oriented close to the line of sight, even if they are in the local Universe (e.g., Meyer et al. 2019).

In this context, the highest redshift flat-spectrum radio quasar (hereafter simply blazar) known to date, PSO J030 947.49+271757.31 (hereafter PSO J0309+27; Belladitta et al. 2020), is the ideal candidate for searching for and studying the emission of jets on the kiloparsec scale in the primordial Universe. To this end, we performed relatively deep *Chandra* X-ray observations (128 ksec; P.I. A. Moretti, Archive Seq. Num. 704032, 704242). PSO J0309+27 was discovered by combining the NRAO VLA Sky Survey (NVSS; at 1.4 GHz; Condon et al. 1998) with the Panoramic Survey Telescope and Rapid Response System (Pan-STARRS; Chambers et al. 2016) and then confirmed spectroscopically (Belladitta et al. 2020). Based on the flat radio spectrum in the 0.15–1.4 GHz observed band and the high X-ray luminosity derived from a *Swift*-XRT observation, this source was classified as a blazar, the first observed at $z > 6$. Thanks to its very bright nature compared to other $z > 6$ AGNs, PSO J0309+27 has been the target of several observational campaigns aimed at constraining the full extent of its spectral energy distribution (SED; see Belladitta et al. 2020, 2021; Spingola et al. 2020; Moretti et al. 2021 and also Mufakharov et al. 2021). In this work we focus on the multiwavelength characterisation of the emission extending a few arcseconds from the AGN position, which was revealed from dedicated X-ray *Chandra* observations and represents the highest redshift jet resolved in X-rays currently known.

In Sect. 2 we present the available radio and optical data that can constrain the arcsecond emission of PSO J0309+27 as well as the X-ray imaging and spectral analysis of the *Chandra* observations. In Sect. 3 we model the X-ray and radio measurements considering both the IC/CMB interaction and the synchrotron emission of a highly energetic population of electrons. We then compare currently available data for the extended jet of PSO J0309+27 to other resolved jets at lower redshift reported in the literature. Finally, in Sect. 4 we summarise our results and conclusions.

Throughout the paper we assume a flat Λ cold dark matter cosmology with $H_0 = 70 \, \mathrm{km \, s^{-1} \, Mpc^{-1}}$, $\Omega_m = 0.3$, and $\Omega_\Lambda = 0.7$, where $1''$ corresponds to a projected distance of 5.66 kpc at $z = 6.1$. Spectral indices are given assuming $S_\nu \propto \nu^{-\alpha}$, and all uncertainties are reported at 90% confidence unless otherwise specified.

2. Multi-wavelength data

In this section we describe the archival and recent proprietary data for PSO J0309+27 relevant to the study of the source's jet at arcsecond resolution. A detailed discussion on the components at scales $\lesssim 1''$ is given by Spingola et al. (2020) in the radio, Belladitta et al. (2021) in the optical to near-infrared (NIR), and Moretti et al. (2021) in X-rays.

2.1. Radio observations

Besides the NVSS survey, PSO J0309+27 was detected in the TIFR Giant Metrewave Radio Telescope Sky Survey (TGSS; Intema et al. 2017) at 150 MHz and in the *Karl G. Jansky* Very Large Array Sky Survey (VLASS; Lacy et al. 2020) at 3 GHz. In both of these surveys an extended component is visible in the north-east (NE) direction. In the TGSS image, the extended structure is possibly observed up to ~20″ (~110 kpc), although the signal-to-noise ratio is low (~2; see Fig. 3 in Belladitta et al.
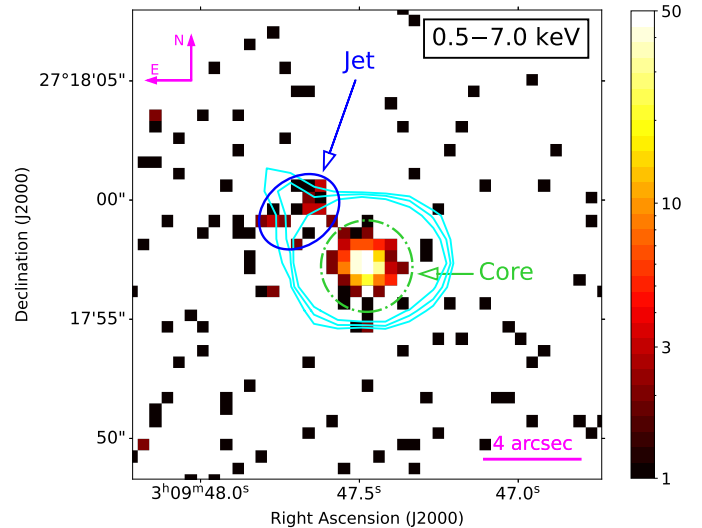
Fig. 1. 3 GHz radio contours from the VLASS survey (in cyan) overlaid on the 0.5–7 keV X-ray image of PSO J0309+27 from the 128 ksec *Chandra* observation. The count colour scale is displayed on the right. For display purposes, only the $(3, 3\sqrt{2}, 6) \times$ the off-source RMS $(=0.12 \, \mathrm{mJy \, beam^{-1}})$ radio contours are reported. The dashed green circle and the solid blue ellipse are the regions used for the extraction of the core and the jet X-ray spectra, respectively.

2020); in the VLASS image the extension is present ~4″ from the core with a significance of approximately five times the RMS: $S_{\mathrm{peak}} = 0.63 \, \mathrm{mJy \, beam^{-1}}$ (RMS = 0.12 mJy beam^{-1}; see Fig. 1). In this work we considered this value for the radio emission of the kiloparsec-scale jet by adding a further 10% to the uncertainty since the VLASS quick-look image flux calibration may be less reliable for faint sources (see Gordon et al. 2020 for more details).

Moreover, PSO J0309+27 was the target of Very Long Baseline Array (VLBA) observations at 1.5, 5, and 8.4 GHz in April 2020. From these radio observations at milliarcsecond angular resolution, Spingola et al. (2020) discovered the presence of a jet that extends for about 500 pc in projection in the NE direction as well (magenta dashed line in Fig. 2). At the same time, low-resolution observations (between 22″ at 1.4 GHz and 1″ at 40 GHz) of PSO J0309+27 with the *Jansky* Very Large Array revealed that the overall radio spectrum of the source is relatively steep ($\alpha_r \sim 1$; Spingola et al. 2020), indicating that its total radio emission is not dominated by the innermost regions of the jet.

2.2. Optical and near-infrared observations

In the optical and NIR bands, the field around PSO J0309+27 was observed in the Pan-STARRS survey (in the g, r, i, z, and Y filters) as well as through dedicated observations with the Telescopio Nazionale *Galileo* (TNG) in the J and K_p filters (P.I. S. Belladitta; see Fig. 2 and Belladitta et al. 2021 for further details). The corresponding 3σ limiting magnitudes for an extended object of the size of the resolved X-ray photons (see Fig. 1 and the next subsection) range from 23.2 to 21.2 mag. In all these observations, as well as in the Wide-field Infrared Survey Explorer Catalogue (CatWISE; Eisenhardt et al. 2020), no optical–IR counterpart associated with the extended jet is observed, suggesting that the observed X-ray emission is likely
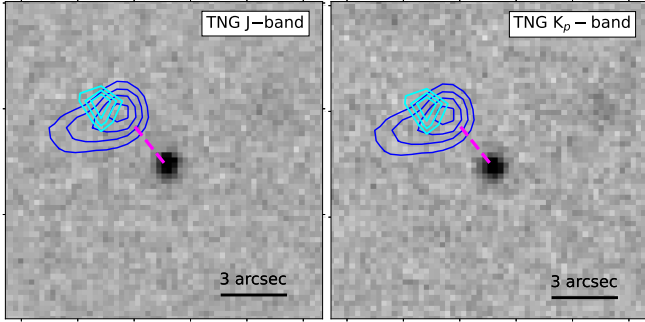
Fig. 2. J- and K_p-band images of PSO J0309+27 obtained with the TNG. The contours of the smoothed *Chandra* X-ray image, with the core's region subtracted, are shown in blue; the contours from the residual VLASS image (i.e. with the core's emission subtracted) are displayed in cyan. The contour levels have been arbitrarily chosen to best show the jet and are always greater than three times the RMS of the given image. The dashed magenta line indicates the direction of the ~500 pc radio jet described in Spingola et al. (2020).

related to the jet of PSO J0309+27 and not to a foreground or background source, such as an obscured active galaxy.

2.3. Chandra X-ray imaging and spectral analysis

2.3.1. Astrometry

PSO J0309+27 has been observed for a total of 128 ksec with the *Chandra* telescope (26.7 ksec in March 2020 and 101.7 ksec in November 2020). Data reduction was performed using the *Chandra* Interactive Analysis of Observations (CIAO) software package (v4.13; Fruscione et al. 2006) with CALDB version 4.9.5. The final image was reconstructed by correcting the astrometry of the single observation segments. To this end, we used the position of five objects detected both in Pan-STARRS and in the *Chandra* observation. The transformation matrix was produced through the wcs_match task. We found typical shifts of +0.7 and +0.9 pixels (1 pixel = 0.492″) in RA and Dec., respectively, with no significant rotation. This is not unexpected given that the overall 68% uncertainty circle of the *Chandra* X-ray absolute position has a radius of 0.6″[1]. Astrometry of the event file and images was modified accordingly by means of the wcs_match task. PSO J0309+27 is detected with 320 photons in the 0.5–7.0 keV band within a 2″ radius circle (98% of the point spread function) with only ~2.7 background photons expected. With the corrected astrometry, the position of the X-ray source is RA = 47.44786 deg and Dec = +27.29922 deg with an error of 0.2″, which is mostly due to the residuals in the astrometric correction. This position is consistent with the Pan-STARRS optical and the VLASS/VLBA radio positions.

2.3.2. X-ray imaging

In Fig. 1 we report the X-ray image obtained from the overall 128 ksec exposure in the 0.5–7 keV energy band with the radio contours at 3 GHz (from the VLASS survey) overlaid. In Fig. 2 we show the residual of the X-ray and radio images after the subtraction of the core emission (assumed to be point-like) overlaid on the NIR images. After the removal of the X-ray core, a significant excess of photons is present between 2″ and 5″ away from the position of PSO J0309+27. Moreover, there is an

overall positional agreement between the extended components in X-rays and in the radio, both directed towards the NE direction, similar to the position angle (PA) of the jet described in Spingola et al. (2020) at parsec scales.

We note that, even though radio data are too shallow for any detailed study, the jet seems to be resolved in X-rays with a lower surface brightness component towards the eastern direction. Such tangential extension could be related to a potential bend at kiloparsec scales. Indeed, if the jet is oriented close to our line of sight (as hinted by the multi-wavelength properties of PSO J0309+27; e.g., Spingola et al. 2020; Moretti et al. 2021), even a small re-orientation of the jet would be amplified through projection and would result in a significant apparent change of direction. Similar bends have already been observed in the jets of several quasars, both at parsec (in the radio band; e.g., Lister et al. 2021) and kiloparsec scales (in the radio and X-ray bands; e.g., Worrall & Birkinshaw 2005; Marshall et al. 2011). Therefore, it is likely that the overall extended X-ray emission of PSO J0309+27 visible in Fig. 2 is associated with different regions of the relativistic jet, before and after the bend. Nevertheless, deeper X-ray and radio observations at arcsecond resolution are needed to confirm this hypothesis and to fully characterise the morphology of this kiloparsec-scale jet. For simplicity, in the following we consider the entire extended emission to be produced in regions with similar physical properties.

In order to qualitatively constrain the projected size of the emitting region, we started by computing the number of photons observed per unit of area around the core of PSO J0309+27 as a function of distance. We show the obtained radial profile in Fig. 3. We also report the expected distribution for a point-like source with an X-ray spectrum given by the core of PSO J0309+27 (see the next subsection). In order to simulate the point spread function (PSF) of the core alone, we used the Model of AXAF Response to X-rays (MARX; version 5.5) *Chandra* end-to-end science simulator through the CIAO task simulate_psf. In particular, we averaged the simulated PSF over 1000 trials with the core's spectrum normalised at 100 times its actual flux as input in order to increase the statistics. From the comparison of the expected PSF and the observed radial distribution, it is clear that up to ~2.5″ PSO J0309+27 is consistent with being a point-like source, whereas at larger radii there is a statistically significant abundance of observed X-ray photons (see Fig. 3, top). In particular, the observed number of photons enclosed in each annulus is five to ten times larger than what is expected from a point source alone.

At the same time, by computing the angular profile of the photons detected in 20 sectors with an inner and outer radius of 2–10″, we find that the observed extended X-ray emission has an angular aperture of ~50 deg centred at a PA of 55 deg. Interestingly, the number of photons observed in the opposite direction, where the counter-jet is expected, is consistent with the background level, thus confirming that we are observing the source at an angle close to the jet's axis. Based on the distributions reported in Fig. 3, throughout the paper we consider the jet to have a radial and angular extension of 2.5″ (from $r = 2.5″$ to $r = 5″$) and 4″ (from PA = 25 deg to PA = 80 deg), respectively. Assuming a viewing angle of $\theta_v \sim 20°$ (see the next section), this projected distance, 15–30 kpc at $z = 6.1$, corresponds to a de-projected size of 40–90 kpc.

2.3.3. X-ray spectral analysis

Based on the values reported in the previous section, the region we adopted for the X-ray spectral analysis is reported with a

---

[1] https://cxc.cfa.harvard.edu/cal/ASPECT/celmon/
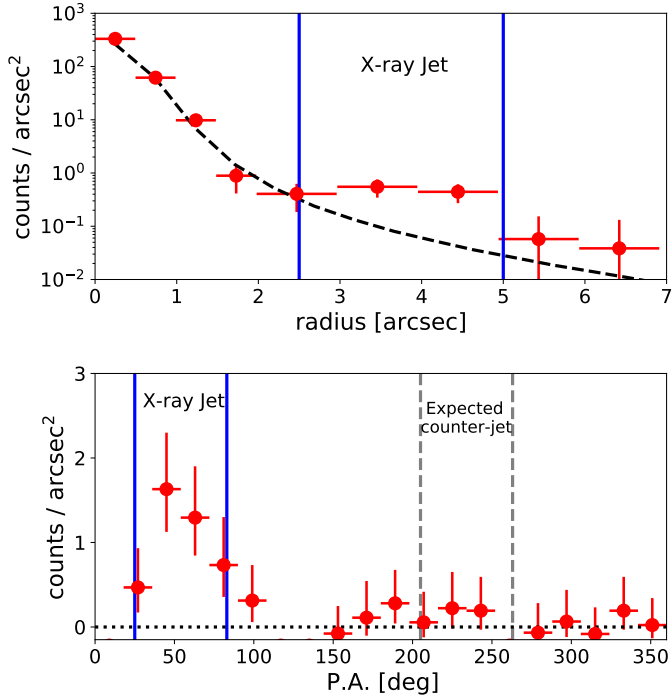
Fig. 3. Observed radial (*top*) and angular (*bottom*) profiles of PSO J0309+27 in the 0.5–7 keV energy band. In both cases the background has been subtracted and data points have Poissonian uncertainties. The dashed black line in the top panel is the expected PSF of the observation, computed with `MARX`. The vertical blue lines delimit the extraction region considered for the spectral analysis of the jet, and the area delimited by the grey lines is where the counter-jet is expected (see Sect. 2.3.2). The direction of the PA in the lower panel is east of north.

solid blue ellipse in Fig. 1 and contains a total of 27 photons between 0.5 and 7 keV.

The analysis of the extended jet was performed in a similar way to the one of the core described in Moretti et al. (2021). Using the `SPECEXTRACT` task, we extracted the core and jet counts from the two regions reported in Fig. 1, while for the background we considered an annulus between 12″ and 25″ centred at the position of the AGN. We then analysed the extracted spectra using the `XSPEC` (v12.11.1) package and performed a fit to both the core and the jet emission in the energy range 0.5–7 keV (in order to reduce the background noise) with a power law absorbed by the Galactic column density along the line of sight ($N_H = 1.13 \times 10^{21}$ cm^{-2}; HI4PI Collaboration 2016) and adopting the C-statistic (Cash 1979). We report in Table 1 the results of the analysis. In the case of the core analysis, the 'flaring' intervals described in Moretti et al. (2021) have not been considered. In Fig. 4 we report the X-ray spectra of the core and the extended jet of PSO J0309+27 modelled as described above.

As already noted by Belladitta et al. (2020), the X-ray properties of the core ($\Gamma_{core} = 1.65$ and $\alpha_{ox} = 1.13$, $\tilde{\alpha}_{ox} = 1.02$[2]) suggest that the observed X-ray emission is dominated by the beamed radiation produced within the jet oriented close to the line of sight (i.e. it is likely a blazar; e.g., Ghisellini 2015; Ighina et al. 2019). The overall X-ray-to-radio ratio ($L_{2-10\,keV}/L_{1.4\,GHz} = 2.76$) is also consistent with the trend of increasing X-ray luminosities as a function of redshift observed up to $z \sim 5.5$ in Ighina et al. (2021), which may be attributed to an

---

[2] Defined as: $\alpha_{ox} = -0.384 \log \frac{L_{2\,keV}}{L_{2500\,\text{Å}}}$ and $\tilde{\alpha}_{ox} = -0.303 \log \frac{L_{10\,keV}}{L_{2500\,\text{Å}}}$.

Table 1. Best-fit parameters derived from the X-ray analysis of both the jet and core component shown in Fig. 1.

	Γ	$f_{0.5-7\,keV}$ (10^{-15} erg s^{-1} cm^{-2})	$L_{2-10\,keV}$ (10^{44} erg s^{-1})	cstat/d.o.f.
Core:	$1.65^{+0.18}_{-0.18}$	$47.82^{+1.21}_{-0.82}$	$78.33^{+17.02}_{-14.01}$	128.9/176
Jet:	$1.79^{+0.74}_{-0.69}$	$3.08^{+0.49}_{-0.30}$	$5.91^{+6.81}_{-3.20}$	26.9/20

Notes. In both cases a simple power law with only Galactic absorption is assumed ($N_H = 1.13 \times 10^{21}$ cm^{-2}; HI4PI Collaboration 2016).
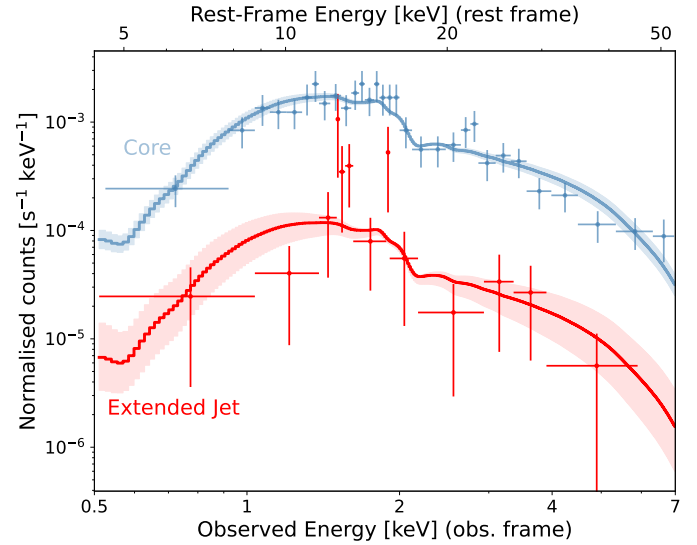
Fig. 4. Folded X-ray spectrum of the core (top, in blue) and of the extended jet (bottom, in red) of PSO J0309+27. Data are binned at a 2σ significance for display purposes only. In both cases data were fitted with a Galactic absorbed power law. The best-fit spectra are reported as solid lines, and the shaded areas represent their 90% confidence uncertainties.

increase in the total X-ray emission (resolved and not) due to the IC/CMB interaction.

The off-nuclear X-ray emission presents a relatively flat slope ($\Gamma_{jet} = 1.79$), which suggests that the population of electrons has not yet suffered significant energy losses (e.g., Achterberg et al. 2001). Its rest-frame luminosity, $L_{2-10\,keV} = 5.91 \times 10^{44}$ erg sec^{-1}, corresponds to ~8% of the core luminosity, making it one of the least core-dominated AGNs detected in X-rays (e.g., Snios et al. 2021) and at the same time one of the most X-ray-luminous extended jets observed to date (e.g., McKeough et al. 2016).

3. Discussion

The mechanism responsible for the high-energy emission observed in large-scale extragalactic jets is still debated. The same electrons emitting in the radio band via the synchrotron process can be responsible for the observed X-ray flux via IC with the CMB photons (e.g., Schwartz et al. 2019). However, this would require that most jets remain relativistic on scales of up to 10–100 kpc (e.g., Tavecchio et al. 2000). As a consequence, one would also expect this same interaction to produce bright γ-ray emission. The non-detection of such radiation with the *Fermi* Large Area Telescope (*Fermi*/LAT) therefore rules

Table 2. Parameters of the model.

Γ_b [1]	θ [2]	γ_{cut} ($\times 10^5$) [3]	K [4]	n_{sh} [5]	B [6]	δ [7]	R [8]	τ_{inj} [9]	t [10]	P_{jet} [11]
1.7	20	4	0.45	2.5	13	2.5	2×10^{21}	5×10^2	10	2.2

Notes. [1]: Jet bulk Lorentz factor; [2]: viewing angle (deg); [3]: cutoff electron Lorentz factor of the shock component; [4]: normalisation of the shock electron energy distribution (particle cm^{-3}); [5]: slope of the shock electron energy distribution; [6]: magnetic field (μG); [7]: Doppler factor; [8]: jet radius (cm); [9]: injection timescales for the shear acceleration in units of the light-crossing time, r_j/c (where r_j is the radius of the jet); [10]: time in units of the light-crossing time, r_j/c. [11]: jet power (10^{46} erg s^{-1}).

out the IC/CMB interaction as the main mechanism responsible for the X-ray radiation produced in the majority of extended jets in the local Universe (e.g., Meyer & Georganopoulos 2014; Meyer et al. 2015). Therefore, another process must be taking place to account for the observed X-ray emission of these jets. The most plausible solution is the presence of a second population of electrons, in addition to the one responsible for the synchrotron radio and IC/CMB X-ray emissions. This population would have to be accelerated to very high energies ($\gamma \sim 10^8$–10^9 or $\sim$100 TeV for magnetic fields of the order of a few microgauss) and then emit in X-rays through the synchrotron process (e.g., Atoyan & Dermer 2004; Kataoka & Stawarz 2005). How these electrons can be accelerated up to very high energies far from the jet launch site is not fully understood yet. In the following we consider the scenario detailed in Tavecchio (2021).

3.1. Two electron population model

The model adopted here for the emission of very high-energy electrons (presented in Tavecchio 2021) is based on the 'shear acceleration' mechanism (e.g., Rieger 2019), in which electrons can be accelerated to ultra-relativistic energies by magnetic turbulence in a shear layer that surrounds the main body of the jet (the spine). This shear layer is expected to be characterised by a strong radial gradient of the velocity. In these conditions, particles diffusing in the layer experience a continuous energy gain through scattering by the turbulence moving at different speeds. An important feature of this model is that the acceleration can only proceed at a sufficiently fast rate in the case of highly energetic electrons. Therefore, this mechanism requires a process able to pre-accelerate the electrons. Possible candidates for the pre-acceleration include turbulence in the flow (Liu et al. 2017) or magnetic reconnection triggered by instabilities at the jet boundary (Sironi et al. 2021). Tavecchio (2021) assumes that electrons experiencing shear acceleration are those accelerated by shocks along the jet (i.e. the ones responsible for the synchrotron emission at low frequency).

Even with a pre-acceleration mechanism, the shear acceleration timescale is relatively long. This feature gives us a simple explanation for the phenomenology observed at both low and high redshift. In fact, at low redshift the relatively small radiative losses allow the electrons in the shear layer to be accelerated up to high energies and therefore to emit in X-rays through a synchrotron process. At high redshift, where the CMB energy density is much higher, the situation changes since the IC/CMB cooling time is significantly shorter than the shear acceleration timescale, even for the most energetic electrons. This severely hampers the acceleration and effectively limits the contribution of the second population to the X-ray emission. At the same time, the increased CMB energy density determines a luminous IC/CMB emission from the low-energy electrons accelerated at the shock, which naturally accounts for the bright X-ray emis-

sion. In this scheme it is therefore natural to expect the second electron population to contribute to or even dominate the X-ray emission of low-z jets, while at high redshift the main contribution derives from the IC/CMB emission of the low-energy electron component.

3.2. Application to PSO J0309+27

PSO J0309+27, with its powerful jet at an unprecedented high redshift, represents the ideal laboratory for testing the scenario presented above. In order to check the consistency with theoretical expectations, we compared our data to the two populations of electrons model used by Tavecchio (2021) to reproduce the emission of the prototypical extended jet associated with the blazar PKS J0637$-$752 at $z = 0.65$. In principle, this model is characterised by many free parameters. However, constraints from jet energetics and acceleration efficiency restrict the range of several parameters. In particular, the magnetic field intensity is constrained by the total energy and cooling of the electrons around 10 μG. Since the treatment of the acceleration is performed in the non-relativistic limit, we assume a relatively small bulk Lorentz factor, $\Gamma_b = 1.7$.

Remarkably, by adopting the same parameter values for the jet characteristics (listed in Table 2) that reproduce the emission of PKS J0637$-$752 at $z = 0.65$ (solid grey line in Fig. 5) and only varying the level of the energy density of the CMB (a factor of $\sim$350 increase from $z = 0.65$ to $z = 6.1$), the same model can also nicely fit the PSO J0309+27 data (solid red line in Fig. 5). In the case of PKS J0637$-$752, the radio and X-ray humps are produced by the synchrotron emissions of the low- and high-energy electron population, respectively. The contribution from the IC/CMB emission of the low-energy electrons is almost negligible (dotted grey lines) up to the hard X-ray band. In the γ-ray band, the model predicts a component due to the combination of synchrotron self-Compton and IC/CMB emission of the high-energy component. However, the absorption of the gamma rays by the extragalactic background light at optical-UV frequencies determines a narrow cutoff around 50 GeV ($\sim$10^{25} Hz). At high redshift (i.e. PSO J0309+27; red lines), the increasing level of the CMB energy density determines the rapid cooling of electrons with Lorentz factors exceeding $\gamma \sim 10^5$. In these conditions the shear acceleration process is basically inactive, while the IC/CMB emission from the low-energy electron component nicely matches the observed X-ray emission.

We note that the relatively small bulk Lorentz factor adopted here is not in contrast with the larger values derived by Spingola et al. (2020) and Moretti et al. (2021) when studying the innermost regions of the jet of PSO J0309+27 in the radio and X-ray band, respectively. This is not unexpected since, at very large distances from the central engine (>1 kpc), the jet likely decelerates (e.g., Bridle et al. 1994; Asada & Nakamura 2012). Otherwise, large bulk Lorentz factors ($\Gamma_b \gtrsim 5$–10)
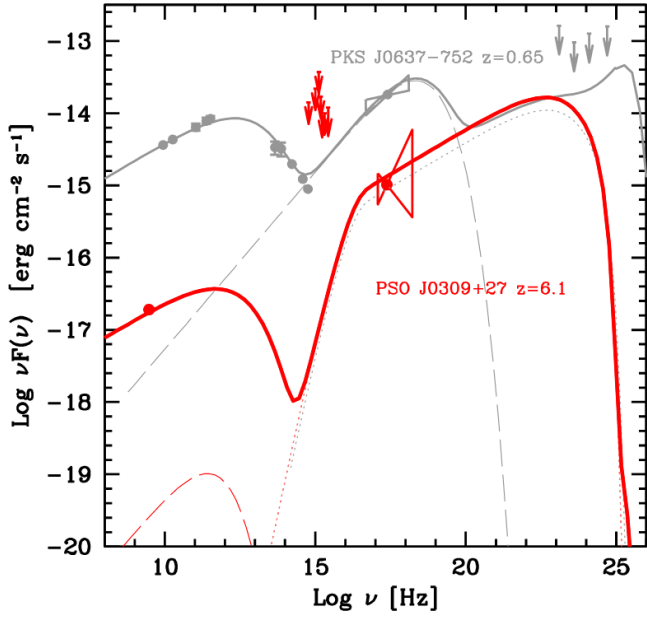
Fig. 5. Observed SED of the extended emission of the source PKS J0637−752 at $z = 0.65$ (grey points), based on which the physical parameters of the model have been set (grey lines). The red lines show the same model but at the redshift of PSO J0309+27, $z = 6.1$. The X-ray, optical-to-NIR, and radio measurements or upper limits of the extended jet emission in PSO J0309+27 are shown as red points and arrows, and those of PKS J0637−752 are shown as grey points and arrows. In grey we also show the upper limits from *Fermi*/LAT for both sources. We stress that the only difference between the input parameters of the two curves is the redshift. At low z the extended X-ray emission is dominated by the synchrotron component (dashed lines) of the second population of electrons accelerated up to ultra-high energies ($\gamma \sim 10^{8-9}$). At high z, on the other hand, electrons are cooled down by the IC/CMB interaction much faster than they can be accelerated, and thus the IC/CMB emission (dotted lines) dominates in the X-rays and the synchrotron emission is significantly quenched.

would imply a strong IC/CMB γ-ray emission detectable by the *Fermi*/LAT, which has not been observed in the majority of the extended jets in the local Universe (e.g., Meyer et al. 2015).

3.3. Redshift evolution of the extended X-ray emission

The two cases analysed in the previous subsection represent two extremes of a continuous sequence regulated by the CMB energy density (i.e. redshift). In order to show the dependence of the kiloparsec-scale jet emission as a function of redshift and to facilitate the comparison with other studies on extended jets, we adopted the X-ray-to-radio flux ratio ($\nu_X S_X / \nu_r S_r$) as well as the corresponding α_{rx} parameter, defined as the slope of a power law connecting the radio and X-ray emission in the observed frame (e.g., Marshall et al. 2005):

$$\alpha_{rx} = -\frac{\log (S_X / S_r)}{\log (\nu_X / \nu_r)} = 1 - \frac{\log (\nu_X S_X / \nu_r S_r)}{\log (\nu_X / \nu_r)}. \quad (1)$$

In both cases, the values are taken at 1 keV and at 3 GHz in the observed frame. The X-ray and radio flux densities of PSO J0309+27 were extracted from the *Chandra* and VLASS images and are reported in Table 3 together with the X-ray-to-radio flux and the jet-to-core (both X-ray and radio) ratios.

In Fig. 6 we show the evolution of the X-ray-to-radio ratio based on the model described above as a function of redshift

(solid red line). As explained in the previous subsection, while at low redshift (PKS J0637−752, orange cross) the high-energy synchrotron emission dominates the observed X-ray range, at high redshift (PSO J0309+27, red star) the only mechanism able to efficiently produce the observed extended X-ray emission is the IC/CMB interaction. Based on the parameters adopted here, the transition between the two mechanisms is expected to be around $z \sim 2$. Beyond this value the peak of the high-energy synchrotron emission shifts below the X-ray band due to cooling, and therefore its contribution to the total radiation observed is negligible (dashed black line). At the same time, the increase in the CMB energy density boosts the IC/CMB emission, which becomes dominant at $z > 2$ (dotted blue line), where we expect to observe its typical evolutionary trend $\propto (1 + z)^{3+\alpha}$ (e.g., Worrall 2009). This is consistent with the other detailed studies on extended jets at $z \sim 3$–4 (e.g., Cheung et al. 2012; Worrall et al. 2020).

In Fig. 6 we also compare the relative X-ray intensity of the extended emission with respect to the radio emission for PSO J0309+27 to the other resolved jets in AGNs at lower redshift available in the literature. All the comparison sources are quasars, as is PSO J0309+27. If the radio data were taken at a different frequency with respect to PSO J0309+27, we computed the corresponding flux density at 3 GHz assuming a radio spectral index of $\alpha_r = 1$, as is typically observed in spatially resolved jets at kiloparsec scales (e.g., Cheung et al. 2006, 2012). The data are largely scattered, probably reflecting the wide variety of the physical properties of the jets and their components. As noted by previous authors (e.g., McKeough et al. 2016; Marshall et al. 2018), although low values of the X-ray-to-radio ratio are not observed at high redshift, the correlation with redshift is not highly significant. In particular, the sources at $z > 2$ do not belong to a single complete sample, and the values reported in the literature are often biased towards objects with a strong X-ray jet since many of them are detections resulted from very short *Chandra* observations (~ 10 ksec; e.g., Snios et al. 2021). As a reference, we also show the limit above which extended jets with similar radio properties to PSO J0309+27 (i.e. radio luminosity) can be detected with a relatively deep (100 ksec) *Chandra* observation (solid green line).

4. Summary and conclusions

In this work we have presented the X-ray detection and analysis of the most distant kiloparsec-scale jet that is spatially resolved, at $z = 6.1$. From dedicated *Chandra* observations we found that the X-ray emission extends up to about $4''$, which is equal to a de-projected linear size of ~ 70 kpc (assuming $\theta_v \sim 20°$). This kiloparsec-scale jet is characterised by a high luminosity ($L_{2-10\,keV} = 5.9^{+6.8}_{-3.2} \times 10^{44}$ erg s^{-1}) as well as one of the largest core-to-jet ratios (8%). Moreover, from the detection of this extended component in the VLASS radio survey, we were also able to constrain its SED and its X-ray-to-radio ratio. The very high redshift of PSO J0309+27 makes it an ideal source for testing the redshift evolution of the emission in extended jets expected from the IC/CMB trend.

By comparing the X-ray-to-radio flux ratio of PSO J0309+27 to the other extended jets analysed in the literature, we found that the value derived for PSO J0309+27 is larger than what is typically measured in the local Universe (e.g., Marshall et al. 2018), as expected from the IC/CMB model. Indeed, assuming physical parameters with values typically seen in the local Universe and only mild relativistic boosting ($\Gamma_b \sim 1.7$), the multi-wavelength emission of the PSO J0309+27 jet is fully consistent with the

Table 3. X-ray and radio properties of the extended jet of PSO J0309+27 extracted from the *Chandra* and VLASS images.

$S_{1\,keV}$ (nJy)	$S_{3\,GHz}$ (mJy)	α_{rx}	$\nu_X S_X / \nu_r S_r$	$(L_{jet}/L_{core})_X$	$(L_{jet}/L_{core})_r$
$0.42^{+0.21}_{-0.18}$	0.63 ± 0.20	-0.78 ± 0.03	54^{+32}_{-29}	8%	5%

Notes. The errors are reported at 90% confidence.
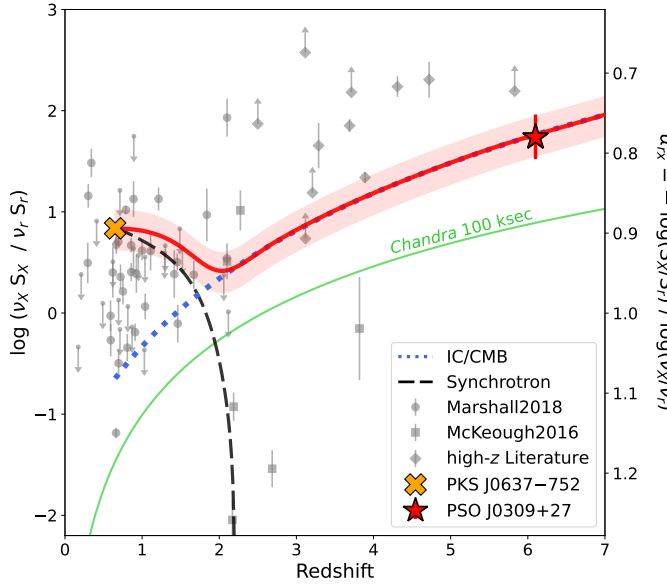
Fig. 6. X-ray-to-radio ratios (and α_{rx}) of the extended jets observed by *Chandra* reported in the literature. The data are from: Marshall et al. (2018), circles at $z \lesssim 2$; McKeough et al. (2016), squares at $2 \lesssim z \lesssim 4.7$ (given by the sum of their 'detected' components); Siemiginowska et al. (2003), Cheung et al. (2006), Simionescu et al. (2016), Schwartz et al. (2020), Worrall et al. (2020), Snios et al. (2021); and Connor et al. (2021), diamonds at $z \gtrsim 3$. If the same object is reported in more than one work, we consider the most recent. PSO J0309+27 ($z = 6.1$) is represented by a red star and PKS J0637−752 ($z = 0.65$) by an orange cross. The solid red line connecting the two sources is the evolution of the X-ray-to-radio ratio as a function of redshift based on the model reported in Fig. 5, where the extended X-ray emission is given by the sum of a synchrotron (dashed black line) and an IC/CMB component (dotted blue line). The solid green line represents the limit above which an extended X-ray jet with the same radio luminosity as the one found in PSO J0309+27 can be observed with a 100 ksec *Chandra* exposure.

IC/CMB interaction of the same electrons responsible for the synchrotron radiation in the radio band.

Although similar conclusions were drawn for a few sources at $z \sim 3$–4 (e.g., Worrall et al. 2020), we also argue that the IC/CMB interaction is the only mechanism able to efficiently produce the extended X-ray emission observed at these redshifts. Indeed, we found that the expected contribution to the extended X-ray emission from a second population of electrons (modelled as discussed in Tavecchio 2021) is naturally quenched at high redshift since the time needed by the electrons to be accelerated up to very high energies becomes longer than the IC/CMB cooling time. In particular, we have shown how the high-energy synchrotron model can reproduce the radio-to-X-ray emission in jets up to $z \sim 2$, after which the redshift dependence of the CMB energy density has a double effect on the two populations of electrons: on the one hand, it enhances the X-ray (and γ-ray) radiation produced through the IC/CMB interaction by the low-energy population; on the other hand, it more efficiently cools the most energetic electrons, which, in turn, cannot be accelerated up to the energies needed to produced synchrotron X-ray emission. Despite the general consistency of this picture with the observations collected so far, detailed studies of statistical samples of high-z jets (with both radio and X-ray data) need to be performed in order to put this result on a more solid basis.

References

Achterberg, A., Gallant, Y. A., Kirk, J. G., & Guthmann, A. W. 2001, MNRAS, 328, 393
Asada, K., & Nakamura, M. 2012, ApJ, 745, L28
Astropy Collaboration (Price-Whelan, A. M., et al.) 2018, AJ, 156, 123
Atoyan, A., & Dermer, C. D. 2004, ApJ, 613, 151
Belladitta, S., Moretti, A., Caccianiga, A., et al. 2020, A&A, 635, L7
Belladitta, S., Caccianiga, A., Diana, A., et al. 2021, A&A, submitted
Bhatta, G., Mohorian, M., & Bilinsky, I. 2018, A&A, 619, A93
Blandford, R., Meier, D., & Readhead, A. 2019, ARA&A, 57, 467
Boccardi, B., Krichbaum, T. P., Ros, E., & Zensus, J. A. 2017, A&ARv, 25, 4
Breiding, P., Meyer, E. T., Georganopoulos, M., et al. 2017, ApJ, 849, 95
Bridle, A. H., Hough, D. H., Lonsdale, C. J., Burns, J. O., & Laing, R. A. 1994, AJ, 108, 766
Cash, W. 1979, ApJ, 228, 939
Celotti, A., Ghisellini, G., & Chiaberge, M. 2001, MNRAS, 321, L1
Chambers, K. C., Magnier, E. A., Metcalfe, N., et al. 2016, ArXiv e-prints [arXiv:1612.05560]
Cheung, C. C., Stawarz, Ł., & Siemiginowska, A. 2006, ApJ, 650, 679
Cheung, C. C., Stawarz, Ł., Siemiginowska, A., et al. 2012, ApJ, 756, L20
Condon, J. J., Cotton, W. D., Greisen, E. W., et al. 1998, AJ, 115, 1693
Connor, T., Bañados, E., Stern, D., et al. 2021, ApJ, 911, 120
Diana, A., Caccianiga, A., Ighina, L., et al. 2021, MNRAS, submitted
Eisenhardt, P. R. M., Marocco, F., Fowler, J. W., et al. 2020, ApJS, 247, 69
Fabian, A. C. 2012, ARA&A, 50, 455
Fabian, A. C., Walker, S. A., Celotti, A., et al. 2014, MNRAS, 442, L81
Fruscione, A., McDowell, J. C., Allen, G. E., et al. 2006, in SPIE Conf. Ser., eds. D. R. Silva, R. E. Doxsey, et al., 6270, 62701V
Georganopoulos, M., Perlman, E. S., Kazanas, D., & McEnery, J. 2006, ApJ, 653, L5
Ghisellini, G. 2015, J. High Energy Astrophys., 7, 163
Gordon, Y. A., Boyce, M. M., O'Dea, C. P., et al. 2020, Res. Notes Am. Astron. Soc., 4, 175
Harris, D. E., & Krawczynski, H. 2002, ApJ, 565, 244
Harris, D. E., & Krawczynski, H. 2006, ARA&A, 44, 463
HI4PI Collaboration (Ben Bekhti, N., et al.) 2016, A&A, 594, A116
Ighina, L., Caccianiga, A., Moretti, A., et al. 2019, MNRAS, 489, 2732
Ighina, L., Caccianiga, A., Moretti, A., et al. 2021, MNRAS, 505, 4120
Intema, H. T., Jagannathan, P., Mooley, K. P., & Frail, D. A. 2017, A&A, 598, A78
Jester, S., Röser, H. J., Meisenheimer, K., & Perley, R. 2002, A&A, 385, L27
Kataoka, J., & Stawarz, Ł. 2005, ApJ, 622, 797
Lacy, M., Baum, S. A., Chandler, C. J., et al. 2020, PASP, 132, 035001
Lister, M. L., Homan, D. C., Kellermann, K. I., et al. 2021, ApJ, 923, 30
Liu, R.-Y., Rieger, F. M., & Aharonian, F. A. 2017, ApJ, 842, 39
Liu, Y., Wang, R., Momjian, E., et al. 2021, ApJ, 908, 124

Marshall, H. L., Schwartz, D. A., Lovell, J. E. J., et al. 2005, ApJS, 156, 13
Marshall, H. L., Gelbord, J. M., Schwartz, D. A., et al. 2011, ApJS, 193, 15
Marshall, H. L., Gelbord, J. M., Worrall, D. M., et al. 2018, ApJ, 856, 66
McKeough, K., Siemiginowska, A., Cheung, C. C., et al. 2016, ApJ, 833, 123
Meyer, E. T., & Georganopoulos, M. 2014, ApJ, 780, L27
Meyer, E. T., Georganopoulos, M., Sparks, W. B., et al. 2015, ApJ, 805, 154
Meyer, E. T., Iyer, A. R., Reddy, K., et al. 2019, ApJ, 883, L2
Moretti, A., Ghisellini, G., Caccianiga, A., et al. 2021, ApJ, 920, 15
Mufakharov, T., Mikhailov, A., Sotnikova, Y., et al. 2021, MNRAS, 503, 4662
Nesvadba, N. P. H., Lehnert, M. D., De Breuck, C., Gilbert, A., & van Breugel, W. 2007, A&A, 475, 145
Rieger, F. M. 2019, Galaxies, 7, 78
Schwartz, D. A., Marshall, H. L., Lovell, J. E. J., et al. 2000, ApJ, 540, 69
Schwartz, D., Siemiginowska, A., Worrall, D., et al. 2019, Astron. Nachr., 340, 30

Schwartz, D. A., Siemiginowska, A., Snios, B., et al. 2020, ApJ, 904, 57
Siemiginowska, A., Smith, R. K., Aldcroft, T. L., et al. 2003, ApJ, 598, L15
Simionescu, A., Stawarz, Ł., Ichinohe, Y., et al. 2016, ApJ, 816, L15
Sironi, L., Rowan, M. E., & Narayan, R. 2021, ApJ, 907, L44
Snios, B., Schwartz, D. A., Siemiginowska, A., et al. 2021, ApJ, 914, 130
Spingola, C., Dallacasa, D., Belladitta, S., et al. 2020, A&A, 643, L12
Tavecchio, F. 2021, MNRAS, 501, 6199
Tavecchio, F., Maraschi, L., Sambruna, R. M., & Urry, C. M. 2000, ApJ, 544, L23
Torres-Albà, N., Bosch-Ramon, V., & Iwasawa, K. 2020, A&A, 635, A57
Weisskopf, M. C., Tananbaum, H. D., Van Speybroeck, L. P., & O'Dell, S. L. 2000, in X-Ray Optics, Instruments, and Missions III, eds. J. E. Truemper, & B. Aschenbach, SPIE Conf. Ser., 4012, 2
Worrall, D. M. 2009, A&ARv, 17, 1
Worrall, D. M., & Birkinshaw, M. 2005, MNRAS, 360, 926
Worrall, D. M., Birkinshaw, M., Marshall, H. L., et al. 2020, MNRAS, 497, 988